nature materials

ARTICLES

https://doi.org/10.1038/s41563-021-00930-7

Three-dimensional nanolithography guided by DNA modular epitaxy

Jie Shen[1,2], Wei Sun[1,2], Di Liu[1,2], Thomas Schaus[1,2] and Peng Yin[1,2] ✉

Lithographic scaling of periodic three-dimensional patterns is critical for advancing scalable nanomanufacturing. Current state-of-the-art quadruple patterning or extreme-ultraviolet lithography produce a line pitch down to around 30 nm, which might be further scaled to sub-20 nm through complex post-fabrication processes. Herein, we report the use of three-dimensional (3D) DNA nanostructures to scale the line pitch down to 16.2 nm, around 50% smaller than state-of-the-art results. We use a DNA modular epitaxy approach to fabricate 3D DNA masks with prescribed structural parameters (geometry, pitch and critical dimensions) along a designer assembly pathway. Single-run reactive ion etching then transfers the DNA patterns to a Si substrate at a lateral critical dimension of 7 nm and a vertical critical dimension of 2 nm. The nanolithography guided by DNA modular epitaxy achieves a smaller pitch than the projected values for advanced technology nodes in field-effect transistors, and provides a potential complement to the existing lithographic tools for advanced 3D nanomanufacturing.

By shaping materials into in-silico-designed patterns with high fidelity, lithography techniques build the manufacturing foundations for electronics[1], photonics[2,3], nanofluidics[4] and nanoelectromechanical systems[5]. In semiconductor processing[6], photolithography has been used over the decades to scale the pitch of gates and contacts (that is, proportionally shrink their centre-to-centre spacing), to meet the projected milestones of integration densities. Recent advances in pitch scaling beyond the diffraction limit of photolithography are mostly ascribed to the multipatterning techniques. For instance, a typical 10-nm node (with a 34-nm fin pitch[7]) uses self-aligned quadruple patterning consisting of six successive steps of deposition and etching. Such complicated processes could increase the risks of patterning failures[8]. Multipatterning techniques also require aligning multiple photolithography layers for scaling pitch and constructing multilayered three-dimensional (3D) patterns, and the alignment accuracy (that is, the overlay control) is limited to 5 nm to date[9]. Alternative patterning approaches, either top-down or bottom-up, have been explored to advance lithography scaling, including extreme-ultraviolet (EUV) lithography[10], e-beam lithography[11], directed self-assembly of block copolymers[12] and nanoimprinting[13]. Despite its costly instruments and reagents, EUV lithography will probably replace quadruple patterning at 30-nm-scale pitches[14]. However, at sub-20-nm-scale pitches, current EUV approaches need to be replaced by either high-numerical-aperture EUV or multipatterning EUV techniques, which are yet to be well established[14].

Through encoding the spatial positioning information into the designable single-stranded DNA (ssDNA) components, structural DNA nanotechnology[15], in particular DNA origami[16–18] and DNA bricks[19–22], enables self-assembly of complex designer DNA nanostructures with single-nanometre feature resolution. This feature allows self-assembled DNA templates to align[23–26] or in-situ synthesize[27,28] inorganic nanostructures in buffer media, at a spatial resolution beyond the pitch limit of photolithography[7,25,26]. Often, however, DNA-directed inorganic nanostructures/patterns cannot be isolated from the underlying DNA templates or buffer to retain intact morphology. Current DNA templates have limited success in dry etching-based lithography, which uses reactive ion etching (RIE) to fabricate freestanding inorganic nanostructures[29,30]. Three technical barriers present challenges to DNA-based lithography. (1) Limited DNA pattern dimensions. Most DNA origami structures are smaller than 0.01 μm² with a monolayer thickness of double-stranded DNA (dsDNA)[31]. Hierarchical self-assembly methods could conjugate DNA origami laterally up to 0.6 μm² in total area[32], but it is hard to stack up multiple DNA origami precisely into a thicker pattern at a high assembly yield. (2) Susceptible 3D DNA nanofeatures. Ordinary RIE masks should be thick enough to resist etchants, but high aspect ratio (height-to-width) DNA nanofeatures often collapse after being dried out of buffer[21,22,33]. (3) Uncontrolled self-assembly pathways. Self-assembly of ssDNAs into micrometre-scaled 3D DNA patterns may involve competing seeding-growth pathways that lower the yield and introduce defects[21,22]. Thus, previous explorations of DNA-based lithography have typically relied on two-dimensional DNA patterns as masks, and have been applied in either wet etching by hydrofluoric acid vapour[33,34] or indirect RIE after coating with metal[29] or silica[35]. Notably, these inorganic coatings sacrifice the spatial resolution of DNA masks.

Herein, we demonstrate scalable 3D nanolithography, which directly uses 3D DNA masks in RIE without any auxiliary inorganic coating (such as metal or silica). We develop a DNA modular epitaxy approach to increase the pattern complexity and lower the structural defects of 3D DNA patterns. The DNA modular epitaxy begins with a flat DNA brick crystal as a substrate, followed by seed-mediated growth of 3D DNA modules on top of the substrate. The assembled 3D DNA masks are stabilized by Ni^{2+} ions, which prevent DNA feature collapse after air-drying on Si substrates. Finally, using the Ni^{2+}-stabilized 3D DNA masks, we apply a single-run RIE to produce the ultra-scaled Si patterns directly. The pitch and the critical dimension (CD, that is, the dimension of the smallest geometrical feature) of Si patterns have been scaled as small as 16.2 ± 0.6 nm and 7.2 ± 1.0 nm, respectively, which is about 50% smaller than current values using quadruple patterning or EUV lithography. Individual 3D DNA masks also enable one-step lithography for multilayered 3D Si patterns at a vertical CD of 2 nm. For future ultra-scaled 3D

[1]Wyss Institute for Biologically Inspired Engineering, Harvard University, Boston, MA, USA. [2]Department of Systems Biology, Harvard Medical School, Boston, MA, USA. ✉e-mail: py@hms.harvard.edu

manufacturing, nanolithography guided by DNA modular epitaxy could potentially complement other conventional lithographic tools for rational shaping of diverse substrates.

Strategy overview

Figure 1 illustrates the workflow of nanolithography guided by DNA modular epitaxy for a multilayered grid pattern. To fabricate such a pattern in silicon, we first designed a 3D DNA mask using 32-nucleotide DNA bricks[20,21]. We then performed a three-stage DNA modular epitaxy assembly in Tris/EDTA/$MgCl_2$ buffer, starting from a DNA substrate (yellow) to 3D modules of taller line (blue) and lower line (green). Next, the as-assembled 3D DNA mask was deposited onto a Si substrate, incubated with $NiCl_2$ solution and then fully dried. After a single-run fluorine-based RIE and the removal of mask residuals, the etched Si pattern exhibited the prescribed multilayered grid geometry.

Mask design details

Figure 2a illustrates the design of an example grid DNA mask (named as 12H-grid). The mask exhibited two layers of cross lines along the *x* and *z* directions, and both layers of lines were designed at an equal pitch (~32 nm). The lines and spaces had equal designed width (~16 nm). We converted the repeating unit of the grid pattern into a unit cell of an *x*–*z*-extending DNA brick crystal[21], as in the LEGO and cylinder model of Fig. 2a (also in Supplementary Fig. 1). The hybridized eight-base pair (B) domain from two neighbouring DNA bricks is designated as a voxel, with a volume of 2.7 nm × 2.4 nm × 2.6 nm (dimension data obtained from liquid-mode atomic force microscopy (AFM), Supplementary Fig. 13). The unit cell consisted of three DNA modules, including the substrate (12 helices (H) × 4H × 94B), the taller line (6H × 8H × 94B) and the lower line (6H × 5H × 47B), as shown in Fig. 2a. The three DNA modules had complementary ssDNAs dangling on their attachment interfaces to propagate the unit cell in the *x*–*z* plane.

DNA modular epitaxy

Controlling seeding and growth pathways can help increase one-pot self-assembly yield of DNA nanostructures[36–39]. However, seeding-growth pathway control for micrometre-scale 3D DNA patterns is still early in its development[21,22]. Inspired by molecular-beam epitaxy of inorganic crystalline films[40] and seed-mediated epitaxial growth of colloidal nanocrystals[41], we developed DNA modular epitaxy to activate a designer seeding-growth pathway along staged 3D DNA self-assembly. Without precisely controlling the assembly dynamics for individual ssDNAs, we designed and controlled ssDNA input order to sequentially grow each 3D DNA module, which simplified the pathway design and improved the yield and the quality for micrometre-scale 3D DNA masks. Figure 2b illustrates the three-stage DNA modular epitaxy for the 12H-grid mask. We first assembled DNA substrates as seeds using concentrated ssDNAs in stage 1, and then introduced other ssDNAs in a stepwise manner to grow DNA line modules in stages 2 and 3. To inhibit the competing seeding pathways in epitaxial growth stages, we gradually decreased the ssDNA concentrations and the reaction temperatures.

In epitaxial stage 1, ssDNA components at an initial concentration of ~310 nM each initiated the seeding of the DNA substrate module (12H × 4H × 94B). The growth of the DNA brick crystal was thermodynamically favourable along the base-pair stacking direction (*z* direction), therefore leaf-like DNA substrates were produced with an average pattern area of ~0.2 ± 0.1 μm × 1.5 ± 0.5 μm (Fig. 2c). Epitaxial stage 2 constructed the taller-line module (6H × 8H × 94B) that propagated along the *z* axis on the DNA substrate. Besides the ssDNA components of the taller-line module (~220 nM each ssDNA), stage 2 introduced a second batch of the substrate ssDNA components to enlarge the dimensions of the DNA substrates. The stage 2 product displayed parallel DNA lines with an average pattern area of 0.3 ± 0.1 μm × 2.5 ± 0.5 μm (Fig. 2c). Epitaxial stage 3 introduced ssDNA components (~180 nM for each) of the lower-line module (6H × 5H × 47B) for assembly. The final product displayed a cross-line grid pattern in scanning electron microscopy (SEM) and AFM images (Fig. 2c,d). We calculated a gross yield of 86%, on the basis of the remaining ssDNA concentration (Supplementary Method 2.6). The cryo-EM image of the DNA mask 12H-grid (Fig. 2e) revealed a single-crystal-like dsDNA lattice with highly ordered 6H-wide lines and 6H-wide spaces. We did not observe blank DNA substrates or discrete DNA lines in products, indicating the effective pathway controllability of DNA modular epitaxy.

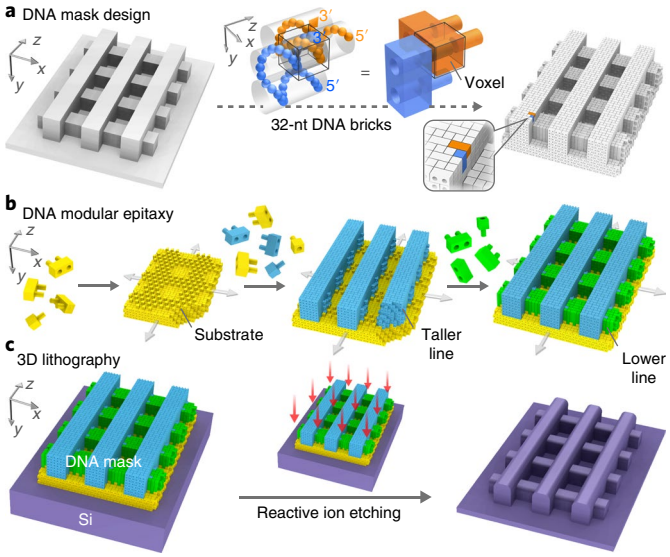

Fig. 1 | Strategy overview. a, In-silico design of a target pattern into a 3D DNA mask from 32-nucleotide (nt) DNA bricks (illustrated by cylinder/strand and LEGO models). **b**, Multistaged DNA modular epitaxy assembly for the 3D DNA mask. The grey arrows indicate the extending directions of the DNA mask. **c**, Pattern transfer to silicon via a single-run RIE.

DNA mask deposition and characterization

Rigid inorganic coating could prevent drying-induced collapse of 3D DNA patterns[21,22,28], but such coating could lower the initial pattern resolution and interfere with subsequent RIE processing. We developed Ni^{2+}-assisted DNA mask deposition to stabilize dried 3D DNA mask patterns on a Si substrate without forming a mineralized inorganic coating. 3D DNA mask solution was first added onto a Si substrate and incubated with $NiCl_2$ solution (50 mM) for 1 hour. Besides promoting DNA mask adsorption onto the Si substrate, Ni^{2+} cations chelated with adjacent DNA helices to enhance the structural stiffness of the 3D DNA modules[42]. After deposition of DNA masks, the Si substrate was rinsed in ethanol to remove water and salt residues while ethanol prevented dsDNA dehybridization. Then, the DNA mask-deposited Si substrate was air-dried to remove all ethanol. Energy dispersive X-ray (EDX) spectroscopy on SEM confirmed that Ni^{2+} ions were homogeneously distributed within the DNA masks at a low dose (Supplementary Method 2.5 and Supplementary Fig. 20).

The Ni^{2+}-chelated 3D DNA mask maintains its intrinsic geometry after being dried. Consider the mask 12H-grid, for example (Extended Data Fig. 1). The SEM line-scan profiles indicated an *x*-axis pitch at 32.3 ± 0.9 nm for the taller lines and a *z*-axis pitch at 32.1 ± 0.9 nm for the lower lines. Their line widths were 13.2 ± 0.6 nm and 12.9 ± 1.0 nm, respectively. AFM profiles indicated three different thicknesses of 4.5 ± 0.3 nm, 14.5 ± 0.9 nm and 19.2 ± 0.7 nm for the DNA substrate, the lower lines and the taller lines, respectively

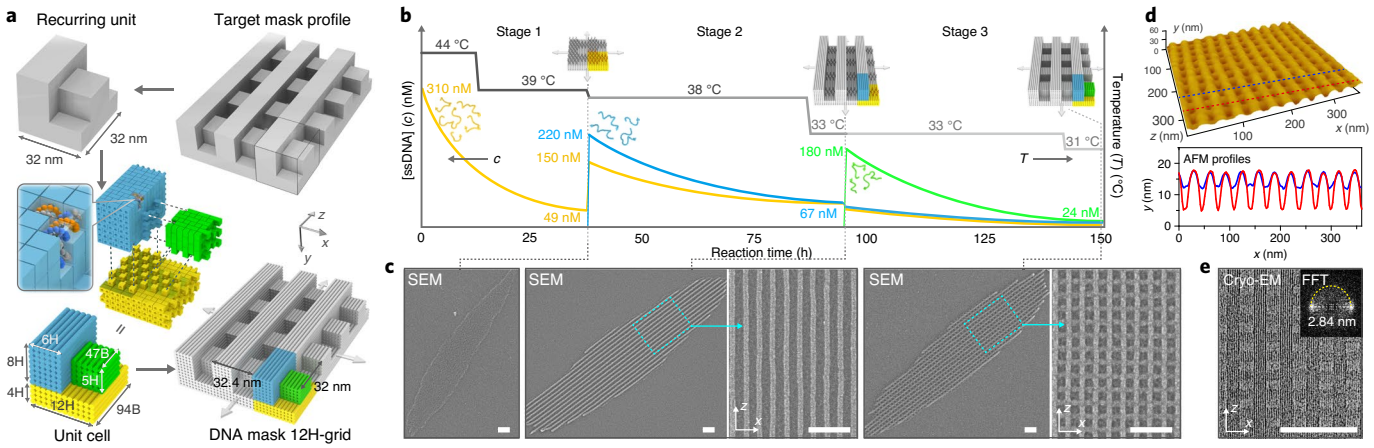

Fig. 2 | DNA modular epitaxy. a, Design for the DNA mask 12H-grid, illustrated by the LEGO model and the cylinder model. **b**, Assembly flowchart for the 12H-grid, together with the measured time course of ssDNA concentrations. **c**, SEM images of the assembled products in each assembly stage. **d**, AFM characterization of the fully dried DNA mask 12H-grid. **e**, Cryo-EM image of the 12H-grid at a resolution of a single dsDNA helix. The highest-intensity spots at ~2.84 nm in the fast Fourier transformation (FFT) patterns of cryo-EM images indicated the effective diameter of the hydrous dsDNA helix. Scale bars, 100 nm.

(Fig. 2d). The increments in AFM-measured line widths came from the artefact of the AFM probe radius.

SEM measurements further showed that the Ni^{2+}-chelated 12H-grid exhibited different drying shrinkages in the mask lines and substrate modules. The DNA substrate was tightly immobilized onto the Si surface and exempted from lateral shrinkage during the drying process, and the DNA substrate maintained a constant *x*-axis pitch of 32.3 ± 0.9 nm for the taller lines (Extended Data Fig. 1d). The corresponding effective *x*-axis diameter of the dried substrate dsDNA was 2.7 nm. In contrast, the *x*-axis width of the freestanding 6H-wide taller line was reduced to 13.2 nm after drying, corresponding to an effective dsDNA diameter of 2.2 nm in the *x* axis (Extended Data Fig. 1c). Because drying shrinkage tensions were proportional to the volumes of 3D DNA modules, the cumulative tensions from the taller lines stretched the lower lines, producing an effective dsDNA diameter of 3.2 nm in the lower lines in the *x* axis. Additionally, our control tests showed that Ni^{2+}-free deposition could induce severe collapse and pitch shrinkages on the mask 12H-b grid (Supplementary Fig. 23).

Mask pattern diversity

On the basis of DNA modular epitaxy, we designed and prepared three commonly used periodic lithographic patterns on DNA masks. The detailed characterization results, including gross yields, dimensions and defect rates, are summarized in Supplementary Tables 1 and 2.

For line/space pattern at a 32-nm pitch, DNA mask 12H-a (Fig. 3a) was composed of a 12H-periodic substrate module (12H × 4H × 94B) and a 6H-wide line module (6H × 8H × 94B). Its two-stage epitaxy assembly resulted in a gross yield of 82%. The DNA lines in the dried mask 12H-a did not collapse on the Si substrate (Supplementary Fig. 4), showing 12.2 ± 0.5 nm in line width and 1.5 nm in line-width roughness (LWR, defined as three times the width standard deviation, see Supplementary Method 2.8). The line pitch of DNA mask 12H-a was 32.2 ± 0.6 nm. At an equivalent line pitch, the LWR of DNA mask 12H-a was smaller than the benchmarking LWR of the EUV lithography resist[43].

DNA mask 12H-pillar (Fig. 3b) exhibited a rectangular array of DNA pillar module (6H × 8H × 47B) on a 12H-periodic substrate (12H × 4H × 94B). The dried mask 12H-pillar had an *x*-axis pitch at 32.5 ± 1.6 nm and a *z*-axis pitch at 32.1 ± 1.9 nm (Supplementary Fig. 12d,g). The DNA pillars measured 16.5 ± 1.1 nm × 19.1 ± 1.1 nm in the *x* and *z* dimensions (Supplementary Fig. 12c,f). The missing or collapsed pillars, defined as feature defects, were around 4.6 defects per μm². At similar pitches and aspect ratios (height/width) of DNA-mask 3D modules, 12H-pillar had more defects than 12H-grid and 12H-a (0.8 and 0 defects per μm²). The large surface-to-volume ratio of DNA pillars probably made them more susceptible to capillary force-induced collapse during the drying process.

Contact hole mask 8H-hole-a was prepared by a subtractive DNA modular epitaxy approach[44], which etched contact holes in a preformed DNA substrate (Fig. 3c). With subtractive DNA modular epitaxy, each hole had well-formed side walls and was free of grain boundary defects (Supplementary Fig. 3). The DNA substrate for 8H-hole-a was prepared by a two-stage additive DNA modular epitaxy, using an *x*–*z* recurring DNA module of 8H × 8H × 94B. In stage 3, we added antisense ssDNAs to etch away a contact hole module of 4H × 8H × 47B in the DNA substrate module, which was driven by hybridization between the substrate DNA bricks and their sequence-complement ssDNAs. The dried DNA mask 8H-hole-a displayed an array of contact holes at an *x*-axis pitch of 21.6 ± 1.0 nm and a *z*-axis pitch of 32.2 ± 0.9 nm (Supplementary Fig. 8d,e). The cross-section dimensions of the holes were measured as 12.4 ± 1.3 nm × 17.9 ± 1.5 nm in the *x*–*z* plane (Supplementary Fig. 8b,c). Some contact holes did not allow an AFM probe to reach the Si substrate beneath (AFM profile in Fig. 3c), probably because of steric hindrance between the AFM probe and the hole side walls.

DNA mask scaling

Figure 4 illustrates the scaling for both the *x*-axis pitches in the line/space DNA masks and the CDs in the contact hole DNA masks. Their epitaxy assembly workflows are summarized in Supplementary Fig. 2. The measurements of DNA masks are summarized in Supplementary Tables 1 and 2.

For line/space patterns, DNA mask 12H-b, designed with the 6H × 12H × 94B line module and the 12H-periodic DNA substrate module, exhibited a pitch of 32.3 ± 0.6 nm and a line width of 14.9 ± 0.4 nm (Extended Data Fig. 2). Compared with 12H-a, 12H-b was 4H taller in its line module, resulting in an increased mask thickness of 24.4 ± 0.7 nm. DNA masks 10H-a (Supplementary Fig. 5) and 10H-b (Extended Data Fig. 3) used the 10H-periodic DNA substrate module (10H × 4H × 94B) to produce 27.0 ± 0.8 nm pitch line/space patterns. Their thickness variation (19.5 ± 0.8 nm and 24.2 ± 0.5 nm) originated from the 4H difference between the line modules 6H × 8H × 94B and 6H × 12H × 94B. DNA masks

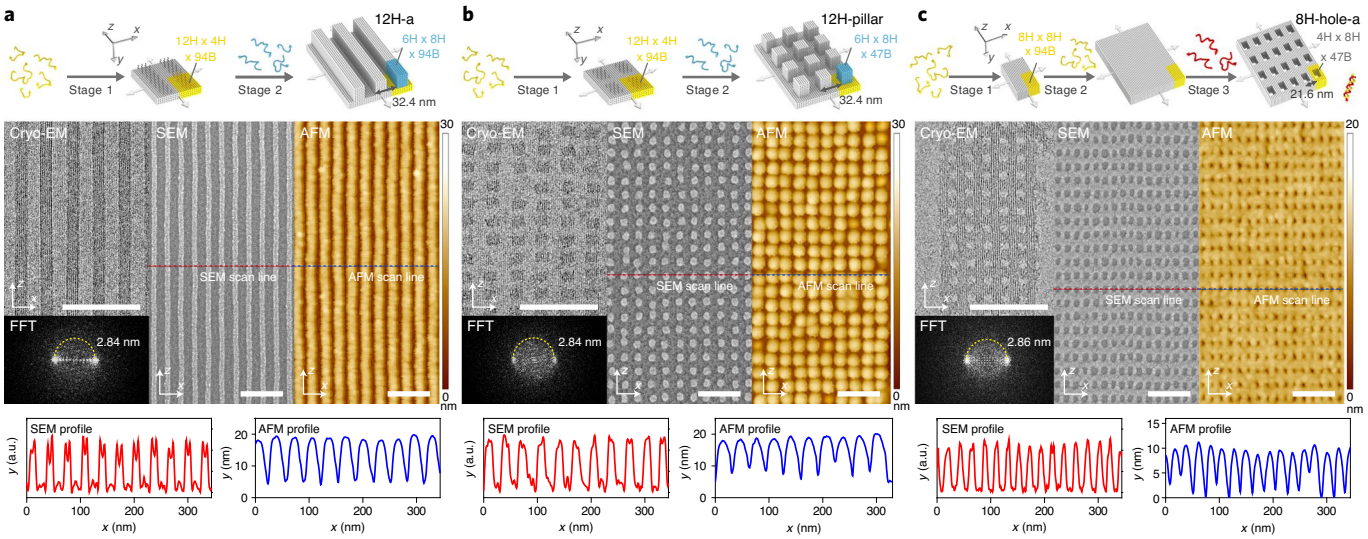

Fig. 3 | Pattern diversity. a–c, Schemes of the DNA modular epitaxy assembly and cryo-EM/SEM/AFM characterizations for line/space mask 12H-a (**a**), pillar array mask 12H-pillar (**b**) and contact hole mask 8H-hole-a (**c**). SEM line-scan profiles were extracted from the red dashed lines. AFM profiles were extracted from the blue dashed lines. Scale bars, 100 nm.

8H-a (Supplementary Fig. 6) and 8H-b (Extended Data Fig. 4) used an 8H-periodic DNA substrate module (8H×4H×94B) to grow 10.4±0.5-nm-wide lines at a pitch of 21.5±0.9 nm. We used the line modules of 4H×6H×94B and 4H×8H×94B to adjust their mask thickness to 15.8±0.7 nm and 18.2±0.7 nm, respectively. DNA mask 6H-a (Supplementary Fig. 7) and 6H-b (Extended Data Fig. 5) produced a 11.0±0.8-nm-wide line (4H×4H×94B) at a pitch of 16.2±0.8 nm. We adjusted the substrate module thickness (6H×4H×94B and 6H×2H×94B) to control their mask thickness to 11.3±0.5 nm and 9.3±0.4 nm, respectively.

The three contact hole masks, 8H-hole-b, 8H-hole-c and 8H-hole-d, were the derivatives of mask 8H-hole-a (Supplementary Fig. 2e). The hole cross-sections of 8H-hole-b, 8H-hole-c and 8H-hole-d were designed as 3H×32B, 3H×24B and 2H×24B in the *x*–*z* plane, respectively. Accordingly, their SEM-measured cross-sectional CDs were 9.3 nm×13.9 nm, 8.5 nm×11.7 nm and 7.9 nm×9.2 nm, respectively (Supplementary Figs. 9–11). All the mask pitch sizes and thicknesses were consistent with the measurements of 8H-hole-a.

Pattern transfer to silicon

Fluorine-based RIE directly transfers the lithographic pattern from a 3D DNA mask to a Si substrate. The DNA 3D features were gradually eroded along the *y* axis and protected the underlying silicon from radical/ion etching. The thickness contrast in the 3D DNA mask (defined as the maximal vertical helices of the DNA mask divided by the vertical helices of its substrate module) led to distinct etching depths in silicon, such that the resulting Si pattern inherited the geometry from the 3D DNA mask. As the scheme in Fig. 5a shows, when RIE etchants depleted the DNA substrate between DNA lines of 12H-b and further etched the underlying silicon, the bottom part of the DNA lines still remained to protect the silicon beneath. The etched Si pattern, named as Si-12H-b, showed parallel Si lines at a pitch of 32.4±0.4 nm (Fig. 5b and Extended Data Fig. 6), which were consistent with the mask geometry. The tilted SEM image indicated the Si lines had no cracks on the top and side walls (Fig. 5c). The EDX mapping test has not detected Ni^{2+} contamination diffused into the Si patterns (Supplementary Fig. 21). Notably, amorphous carbon or a SiO_2 layer sandwiched between the DNA mask and Si substrate might provide facile prevention of metal ion diffusion during RIE.

The RIE process was implemented using 5 sccm (standard cubic centimetres per minute) of CHF_3, 13 mbar of chamber pressure, 200 W of coil power and 10 W of plate power. This RIE protocol produced a vertical etching rate of 12 nm min^{-1} in silicon, with a Si-to-DNA etching selectivity (ratio of etching rates) above 1. The optimization of RIE parameters considered the following guidelines. (1) Feed gas species. Compared with SF_6 and CF_4, we found CHF_3 had the best etching controllability on DNA masks due to its low output of fluorine radicals. Additionally, CHF_3 provided more polymeric fluorocarbon by-products to stabilize DNA masks[45]. (2) Gas flow and pressure. Both parameters were proportional to radical concentrations and inversely proportional to mean free paths of bombarding ions. Optimizing these two parameters could adjust the radical/ion ratio for balancing radical-directed chemical-selective etching and ion-directed anisotropic physical etching. (3) Coil and plate power. The operating power of inductively coupled plasma coils and plate electrodes determined the etchants yield and the ion bombarding energy, respectively. The etchants yield and the ion bombarding energy were responsible for the fine adjustment to chemical/physical etching activities to maximize Si-to-DNA etching selectivity and etching smoothness.

Silicon pattern scaling

The etched Si pattern products from single-run RIE demonstrated the rational scaling of pitches and CDs (see detailed measurements in Supplementary Table 3). Figure 5d illustrates SEM and AFM images of Si line/space patterns (Si-12H-b, Si-10H-b, Si-8H-b and Si-6H-b, named after the corresponding DNA masks) at the prescribed pitches of 32.3±0.4 nm, 27.0±0.4 nm, 21.6±0.6 nm and 16.2±0.6 nm, respectively (Extended Data Figs. 6–9). Radical-directed side-wall etching made the etched Si lines slightly narrower than the DNA mask lines. For example, the CD line widths of DNA mask 12H-b and the corresponding RIE product Si-12H-b were 14.9±0.4 nm and 12.2±0.4 nm, respectively. On the basis of the Si line height in Si-12H-b (35.5±0.7 nm) and the DNA line height in mask 12H-b (24.4±0.7 nm), the aspect ratio (height/width) for the etched Si line was 3, and the Si-to-DNA etching selectivity was 1.4.

The Si hole patterns, including Si-hole-a, Si-hole-b, Si-hole-c and Si-hole-d, displayed an *x*-axis pitch at 21.6±0.7 nm and a *z*-axis pitch at 32.2±0.9 nm, both values consistent with the geometries of DNA

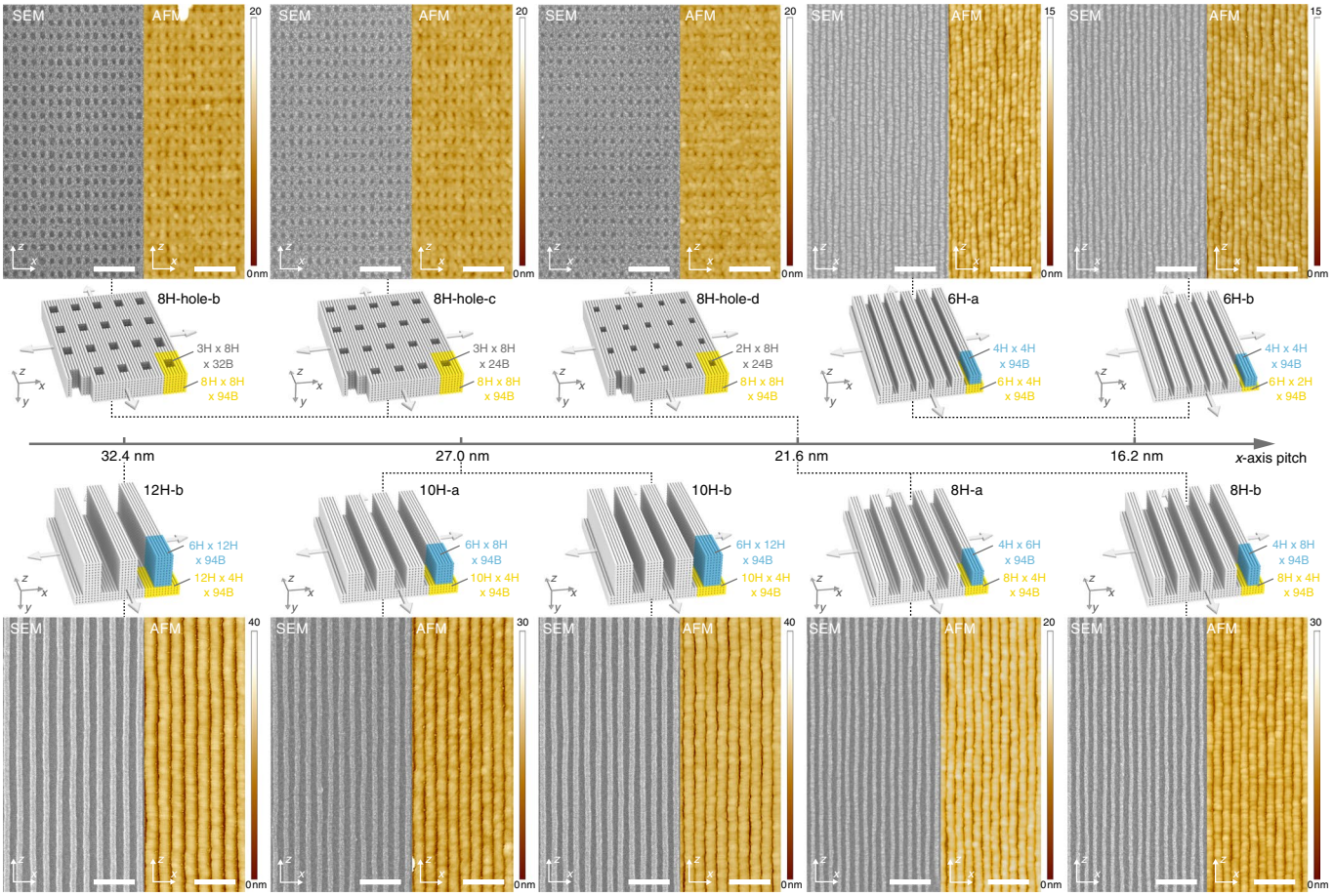

Fig. 4 | Scaling pitch and CD of DNA masks. Schematic structures and SEM/AFM characterization results for DNA masks with prescribed pitches and CDs, listed in an order of down-scaled *x*-axis pitches. Scale bars, 100 nm.

masks. The cross-sectional CDs of Si holes were sequentially scaled to 12.8 nm × 19.2 nm, 10.7 nm × 15.4 nm, 8.3 nm × 12.1 nm and 7.2 nm × 8.6 nm along the *x* and *z* axes (Fig. 5e–g; Supplementary Figs. 16–19).

We also adjusted CDs of Si lines by controlling radical-dominant side-wall etching for DNA masks 8H-b. We mixed H_2 into CHF_3 gas to decrease its radical yield, while ion-directed vertical etching maintained its original efficiency (Fig. 5h). The decrease of radical concentration then led to side-wall deposition of fluorocarbon polymers and increased the effective CD of DNA lines (Fig. 5i). Therefore, the CDs (widths) of Si lines were proportionally increased from 11.4 ± 0.6 to 13.6 ± 0.6 nm by raising the H_2 flow rate from 0 to 1 sccm (Fig. 5j,k; Supplementary Figs. 14 and 15).

High-resolution 3D lithography

The conventional single-mask 3D lithography methods, such as greyscale e-beam or greyscale ultraviolet lithography, are limited to submicrometre-level vertical (*y* axis) CDs in patterning polymer resists[46]. Therefore, for manufacturing multilayered 3D Si nanostructures, overlaying multiple layers of planar mask/pattern via repeating lithography-etching processes is required. Here we demonstrated a direct 3D nanolithography with single-run RIE, which transfers the precise thickness contrast of an individual DNA mask into multilayered 3D Si nanostructures (Extended Data Fig. 10). The model DNA mask, the 12H-grid, had three-layered geometry, and the thickness difference between the taller line and lower line was 4.7 nm. Using the model DNA masks, Fig. 6a,b illustrates the time-series RIE process of 3D Si pattern formation. The final Si pattern displayed three-layered cross-line grid geometry, with feature heights of 6.1 ± 0.9 nm, 17.5 ± 0.8 nm and 19.6 ± 0.6 nm for the space, lower lines and taller lines, respectively (Fig. 6c,d). The 2-nm height difference between the taller and lower Si lines demonstrated the vertical CD (or *y*-axis resolution) of our 3D nanolithography for silicon processing. Tilted SEM imaging showed the lower lines had stochastic cracks with a defect rate of 8.1 per μm² (Fig. 6f). These defects were inherited from DNA line breaks induced by DNA shrinkage tension and RIE heating effects. Introducing poly-T oligonucleotides as elastic spacers within the lower-line DNA module, and using cryogenic RIE instead, could potentially solve this problem.

Outlook

Complex component interactions during 3D DNA self-assembly produce diverse possible assembly pathways. The DNA modular epitaxy approach simplifies a complicated 3D DNA pattern into several basic 3D modules, and then prescribes a sequential order to assemble these modules. In isolated stages of DNA modular epitaxy, reaction temperature and ssDNA concentrations are readily adjusted to facilitate a single seeding-growth pathway. Therefore, DNA modular epitaxy could be experimentally implemented via a designer seeding-growth pathway, and enables more complicated ssDNA components and pattern geometries to facilitate nanolithography. For instance, we raised the thickness contrast of line/space DNA masks to improve the height/width aspect ratios and the LWR of etched Si lines, as in the measurements of Si-12H-a/Si-12H-b and Si-6H-a/Si-6H-b shown in Supplementary Table 3. We could develop even thicker DNA modules to increase mask thickness contrast in future studies. Optionally, we could use a

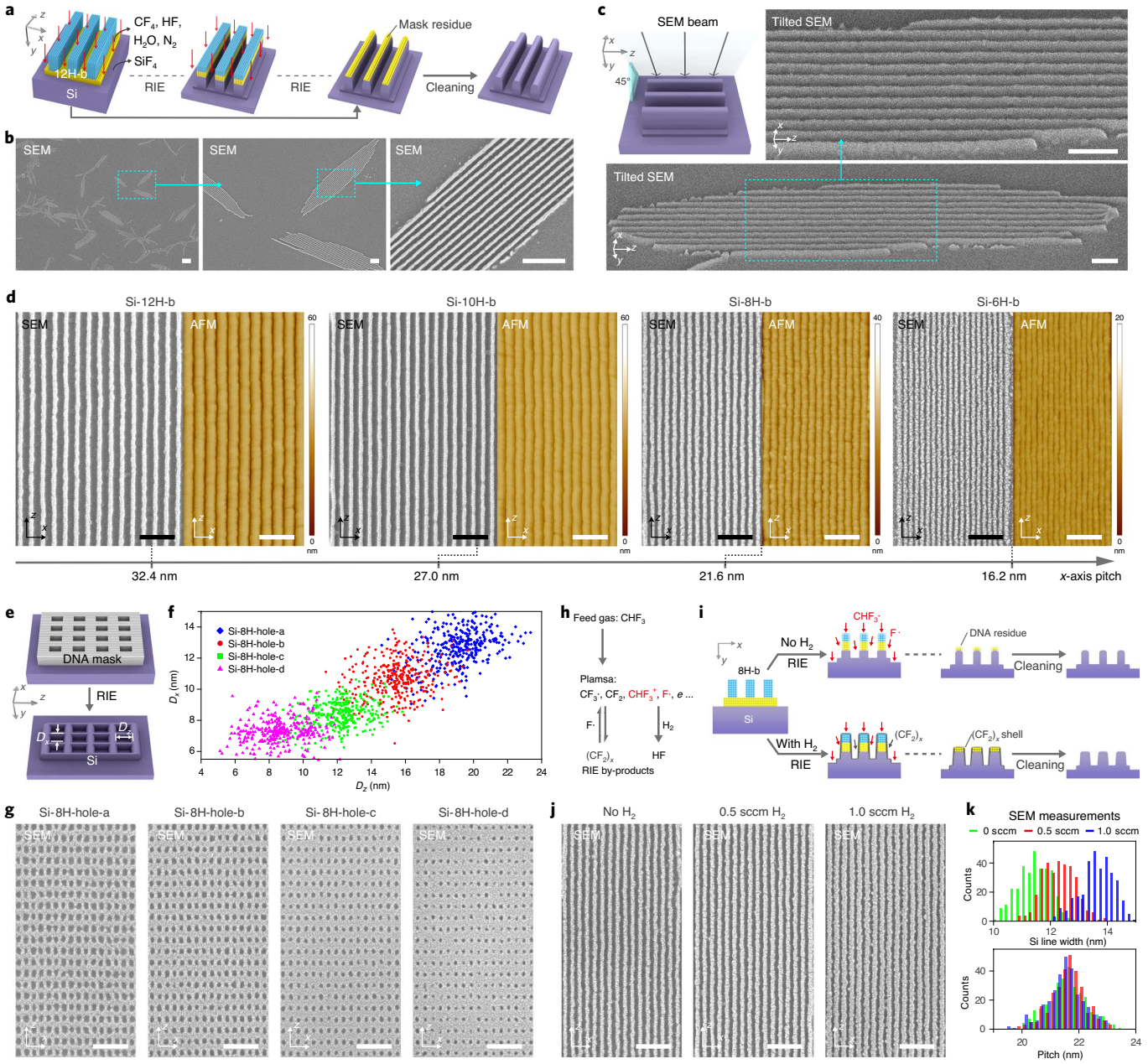

Fig. 5 | Pattern transfer to silicon. a, Schematic mechanism of single-run RIE with DNA mask 12H-b. **b**, SEM images of the etched Si patterns, Si-12H-b. **c**, Tilted SEM images of Si-12H-b pattern. **d**, SEM and AFM images of line/space Si patterns Si-12H-b, Si-10H-b, Si-8H-b and Si-6H-b, respectively. **e**, Schematic of DNA contact hole mask and the etched Si pattern, D_x and D_z are the hole diameters along the *x* and *z* axes. **f**,**g**, Statistical CD analysis (**f**) and SEM images (**g**) of Si hole patterns Si-8H-hole-a, Si-8H-hole-b, Si-8H-hole-c and Si-8H-hole-d, respectively. **h**,**i**, Schematic mechanism of etchants conversion (**h**) and etchants interactions with the 3D DNA mask (**i**) during the hydrogen-mediated RIE process. **j**, SEM images of serial Si line/space patterns etched from DNA mask 8H-b. **k**, SEM measurements of line widths and pitches. Scale bars are 1 μm, 200 nm and 200 nm in **b**. All other scale bars are 100 nm.

supercritical CO_2 rinsing method to reduce the risk of capillary collapse[47].

Using DNA modular epitaxy-assembled DNA patterns as lithography masks, our DNA nanolithography enables the following. (1) High-precision pitch scaling. DNA modular epitaxy scales the line pitch of 3D DNA masks to 16.2 nm with a standard deviation below 1.0 nm. Through one-step RIE, the Si patterns inherit such low standard deviation pitch values from the 3D DNA masks. (2) High-resolution 3D lithography. Besides the scaling of pitches and CDs, DNA modular epitaxy precisely controls the thickness of multilayered 3D DNA masks, resulting in multilayered Si nanostructures at a vertical CD of 2 nm, from an individual mask and a single-run RIE.

The next step for nanolithography guided by DNA modular epitaxy would be wafer-scale registration with DNA mask arrays. One promising approach for wafer-scale registration is through aligning pre-assembled DNA masks onto a prepatterned substrate[25,26,48]. In particular, surface-aligned monodispersed sub-100-nm DNA structures could be used as seeds for DNA modular epitaxy. This route could enable us to construct non-periodic DNA masks at prescribed positions over a wafer-scale substrate.

Nanolithography guided by DNA modular epitaxy bridges biomolecule self-assembly and RIE manufacturing. In addition to silicon, this lithography method could be applied to other RIE substrates. Additionally, 3D DNA masks could be used in chemical

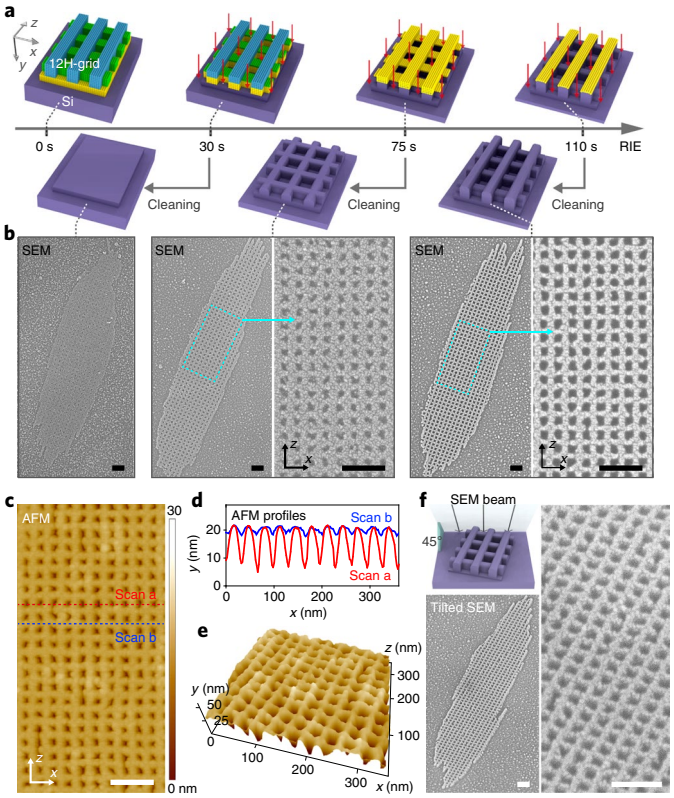

Fig. 6 | 3D lithography with single DNA mask. a,**b**, Schematic (**a**) and SEM characterization (**b**) of the time-series RIE products from the DNA mask 12H-grid. **c**–**f**, AFM image (**c**), AFM line-scan profiles (**d**), 3D AFM image (**e**) and tilted SEM images (**f**) of the etched silicon pattern Si-12H-grid. Scale bars, 100 nm.

vapour deposition[35], physical vapour deposition[49] and atomic layer deposition[50]. For future ultra-scaled 3D devices, DNA modular epitaxy may complement existing nanomanufacturing approaches[2,4].

Online content

Any methods, additional references, Nature Research reporting summaries, source data, extended data, supplementary information, acknowledgements, peer review information; details of author contributions and competing interests; and statements of data and code availability are available at https://doi.org/10.1038/s41563-021-00930-7.

Received: 6 March 2020; Accepted: 14 January 2021;
Published online: 12 April 2021

References

1. Lu, W. & Lieber, C. M. Nanoelectronics from the bottom up. *Nat. Mater.* **6**, 841–850 (2007).
2. Soukoulis, C. M. & Wegener, M. Past achievements and future challenges in the development of three-dimensional photonic metamaterials. *Nat. Photon.* **5**, 523–530 (2011).
3. Kildishev, A. V., Boltasseva, A. & Shalaev, V. M. Planar photonics with metasurfaces. *Science* **339**, 1232009 (2013).
4. Fu, J., Schoch, R. B., Stevens, A. L., Tannenbaum, S. R. & Han, J. A patterned anisotropic nanofluidic sieving structure for continuous-flow separation of DNA and proteins. *Nat. Nanotechnol.* **2**, 121–128 (2007).
5. Loh, O. Y. & Espinosa, H. D. Nanoelectromechanical contact switches. *Nat. Nanotechnol.* **7**, 283–295 (2012).
6. Chau, R. et al. Benchmarking nanotechnology for high-performance and low-power logic transistor applications. *IEEE Trans. Nanotechnol.* **4**, 153–158 (2005).
7. James, D. *IEDM 2017: Intel's 10 nm Platform Process* (2017); https://sst.semiconductor-digest.com/chipworks_real_chips_blog/2017/12/
8. Vincent, B., Lariviere, S., Wilson, C., Kim, R. H. & Ervin, J. Virtual fabrication and advanced process control improve yield for SAQP process assessment with 16 nm half-pitch. In *Proc. SPIE, Adv. Etch. Technol. Nanopatterning VIII* 109630Q (SPIE, 2019).
9. *The International Technology Roadmap for Semiconductors 2.0: 2015 Edition* (Semiconductor Industry Association, 2015).
10. Wagner, C. & Harned, N. EUV lithography: lithography gets extreme. *Nat. Photon.* **4**, 24–26 (2010).
11. Chen, Y. Nanofabrication by electron beam lithography and its applications: a review. *Microelectron. Eng.* **135**, 57–72 (2015).
12. Park, M., Harrison, C., Chaikin, P. M., Register, R. A. & Adamson, D. H. Block copolymer lithography: periodic arrays of 10^{11} holes in 1 square centimeter. *Science* **276**, 1401–1404 (1997).
13. Chou, S. Y., Krauss, P. R. & Renstrom, P. J. Imprint lithography with 25-nanometer resolution. *Science* **272**, 85–87 (1996).
14. Wu, B. & Kumar, A. Extreme ultraviolet lithography and three dimensional integrated circuit—a review. *Appl. Phys. Rev.* **1**, 011104 (2014).
15. Seeman, N. C. DNA in a material world. *Nature* **421**, 427–431 (2003).
16. Rothemund, P. W. K. Folding DNA to create nanoscale shapes and patterns. *Nature* **440**, 297–302 (2006).
17. Douglas, S. M. et al. Self-assembly of DNA into nanoscale three-dimensional shapes. *Nature* **459**, 414–418 (2009).
18. Dietz, H., Douglas, S. M. & Shih, W. M. Folding DNA into twisted and curved nanoscale shapes. *Science* **325**, 725–730 (2009).
19. Wei, B., Dai, M. J. & Yin, P. Complex shapes self-assembled from single stranded DNA tiles. *Nature* **485**, 623–626 (2012).
20. Ke, Y., Ong, L. L., Shih, W. M. & Yin, P. Three-dimensional structures self-assembled from DNA bricks. *Science* **338**, 1177–1183 (2012).
21. Ke, Y. et al. DNA brick crystals with prescribed depths. *Nat. Chem.* **6**, 994–1002 (2014).
22. Ong, L. L. et al. Programmable self-assembly of three-dimensional nanostructures from 10,000 unique components. *Nature* **552**, 72–77 (2017).
23. Maune, H. T. et al. Self-assembly of carbon nanotubes into two-dimensional geometries using DNA origami templates. *Nat. Nanotechnol.* **5**, 61–66 (2009).
24. Liu, N. & Liedl, T. DNA-assembled advanced plasmonic architectures. *Chem. Rev.* **118**, 3032–3053 (2018).
25. Sun, W. et al. Precise pitch-scaling of carbon nanotube arrays within three-dimensional DNA nanotrenches. *Science* **368**, 874–877 (2020).
26. Zhao, M. et al. DNA-directed nanofabrication of high-performance carbon nanotube field-effect transistors. *Science* **368**, 878–881 (2020).
27. Sun, W. et al. Casting inorganic structures with DNA molds. *Science* **346**, 1258361 (2014).
28. Liu, X. et al. Complex silica composite nanomaterials templated with DNA origami. *Nature* **559**, 593–598 (2018).
29. Jin, Z. et al. Metallized DNA nanolithography for encoding and transferring spatial information for graphene patterning. *Nat. Commun.* **4**, 1663 (2013).
30. Shen, B. et al. Plasmonic nanostructures through DNA-assisted lithography. *Sci. Adv.* **4**, eaap8978 (2018).
31. Hong, F., Zhang, F., Liu, Y. & Yan, H. DNA origami: scaffolds for creating higher order structures. *Chem. Rev.* **117**, 12584–12640 (2017).
32. Tikhomirov, G., Petersen, P. & Qian, L. Fractal assembly of micrometre-scale DNA origami arrays with arbitrary patterns. *Nature* **552**, 67–71 (2017).
33. Diagne, C. T., Brun, C., Gasparutto, D., Baillin, X. & Tiron, R. DNA origami mask for sub-ten-nanometer lithography. *ACS Nano* **10**, 6458–6463 (2016).
34. Surwade, S. P., Zhao, S. & Liu, H. Molecular lithography through DNA-mediated etching and masking of SiO_2. *J. Am. Chem. Soc.* **133**, 11868–11871 (2011).
35. Surwade, S. P. et al. Nanoscale growth and patterning of inorganic oxides using DNA nanostructure templates. *J. Am. Chem. Soc.* **135**, 6778–6781 (2013).
36. Schulman, R. & Winfree, E. Synthesis of crystals with a programmable kinetic barrier to nucleation. *Proc. Natl Acad. Sci. USA* **104**, 15236–15241 (2007).
37. Barish, R. D., Schulman, R., Rothemund, P. W. K. & Winfree, E. An information-bearing seed for nucleating algorithmic self-assembly. *Proc. Natl Acad. Sci. USA* **106**, 6054–6059 (2009).
38. Woods, D. et al. Diverse and robust molecular algorithms using reprogrammable DNA self-assembly. *Nature* **567**, 366–372 (2019).
39. Zhang, Y., Reinhardt, A., Wang, P., Song, J. & Ke, Y. Programming the nucleation of DNA brick self-assembly with a seeding strand. *Angew. Chem. Int. Ed. Engl.* **132**, 8594–8600 (2020).
40. Hooks, D. E., Fritz, T. & Ward, M. D. Epitaxy and molecular organization on solid substrates. *Adv. Mater.* **13**, 227–241 (2001).
41. Peng, X., Schlamp, M. C., Kadavanich, A. V. & Alivisatos, A. P. Epitaxial growth of highly luminescent CdSe/CdS core/shell nanocrystals with photostability and electronic accessibility. *J. Am. Chem. Soc.* **119**, 7019–7029 (1997).

42. Choi, J. K., Sargsyan, G., Shabbir-Hussain, M., Holmes, A. E. & Balaz, M. Chiroptical detection of condensed nickel(II)-Z-DNA in the presence of the B-DNA via porphyrin exciton coupled circular dichroism. *J. Phys. Chem. B* **115**, 10182–10188 (2011).
43. Raley, A., Mack, C., Thibaut, S., Liu, E. & Ko, A. Benchmarking of EUV lithography line/space patterning versus immersion lithography multipatterning schemes at equivalent pitch. In *Proc. SPIE, International Conference on Extreme Ultraviolet Lithography 2018* 1080915 (SPIE, 2018).
44. Wei, B., Ong, L. L., Chen, J., Jaffe, A. S. & Yin, P. Complex reconfiguration of DNA nanostructures. *Angew. Chem. Int. Ed. Engl.* **53**, 7475–7479 (2014).
45. Rueger, N. R. et al. Role of steady state fluorocarbon films in the etching of silicon dioxide using CHF_3 in an inductively coupled plasma reactor. *J. Vac. Sci. Technol. A* **15**, 1881–1889 (1997).
46. Khazi, I., Muthiah, U. & Mescheder, U. 3D free forms in c-Si via grayscale lithography and RIE. *Microelectron. Eng.* **193**, 34–40 (2018).
47. Yamazaki, K., Kurihara, K., Namatsu, H., Yamazaki, K. & Kurihara, K. Supercritical resist dryer. *J. Vac. Sci. Technol. B* **18**, 780–784 (2000).
48. Gopinath, A., Miyazono, E., Faraon, A. & Rothemund, P. W. K. Engineering and mapping nanocavity emission via precision placement of DNA origami. *Nature* **535**, 401–405 (2016).
49. Brun, C. et al. Metallic conductive nanowires elaborated by PVD metal deposition on suspended DNA bundles. *Small* **13**, 1700956 (2017).
50. Zhou, F. et al. Programmably shaped carbon nanostructure from shape-conserving carbonization of DNA. *ACS Nano* **10**, 3069–3077 (2016).

Methods

3D DNA mask preparation. The DNA mask 12H-grid was synthesized by the following procedure. At epitaxial stage 1, ssDNA components of the substrate (~310 nM each) were mixed into 16 µl TE/Mg^{2+} buffer (5 mM Tris, 1 mM EDTA and 40 mM $MgCl_2$, pH 7.9). The mixture was sequentially incubated at 44 °C for 12 h and 39 °C for 24 h. At epitaxial stage 2, ssDNA components of the substrate (~190 nM each) and the taller line (~280 nM each) were mixed into the 54 µl TE/Mg^{2+} buffer and added into the product solution of stage 1. Then, their corresponding effective ssDNA concentrations were ~150 nM and ~220 nM, respectively. The mixture was sequentially incubated at 38 °C for 48 h and 33 °C for 8 h. At epitaxial stage 3, ssDNA components of the lower line were mixed in 13 µl of TE/Mg^{2+} buffer, and added into the product solution of stage 2 (~180 nM each). The mixture was incubated sequentially at 33 °C for 48 h and 31 °C for 8 h. The epitaxy products were stored in the reaction buffer and kept at 4 °C without further purification.

Pattern transfer to silicon. The 100-fold diluted 3D DNA mask (2 µl, 10 mM $MgCl_2$) was added onto a 5 mm × 5 mm Si substrate and incubated with $NiCl_2$ solution (2 µl, 100 mM) for 1 h. Then, the DNA mask-deposited Si substrate was rinsed sequentially in 70%, 90% and 99.5% ethanol, followed by drying in air. Without further treatment, the DNA mask-deposited Si substrate was sent to an inductively coupled plasma etching system (STS ICP-RIE) for pattern transfer. The etched Si substrate was sonicated in acetone and then washed in a hot piranha solution (a mixture of 98% sulfuric acid and 25% hydrogen peroxide in a 3:1 volume ratio) to remove the residual DNA masks and fluorocarbon polymers. The cleaned Si substrate was rinsed by deionized water and dried in air for AFM and SEM characterizations.

Defect rate analysis. The defects of dried 3D DNA masks and Si pattern products were counted by SEM. For each sample, we randomly selected 20 pieces of discrete DNA or Si patterns within a 100-µm scale region, and calculated the ratio of the amount of defects versus the sum of the pattern area. The overlapped and upside-down laid DNA masks, and their corresponding RIE products, were not involved in defect counting (examples are shown in Supplementary Fig. 22).

Data availability

The data that support the findings of this study are available within the article and its Supplementary Information files and from the corresponding authors upon reasonable request.

References

51. Shen, J., Sun, W. & Yin, P. Scalable nucleic acid-based nanofabrication. US patent 2017/0190573 A1 (2017).

Acknowledgements

We thank J.D. Deng, L. Xie and S. Stoilova-McPhie at the Center for Nanoscale Systems of Harvard University for valuable discussion and help with cryo-EM work. This work is supported by NSF (CMMI-1333215, CMMI-1344915 and CBET-1729397), AFOSR (MURI FATE, FA9550–15–1–0514) and internal funding support from the Wyss Institute to P.Y. D.L. is supported by a Merck Fellowship of the Life Sciences Research Foundation.

Author contributions

J.S. conceived, designed and conducted the lithography study and wrote the manuscript. W.S. conceived, designed and conducted the DNA modular epitaxy study and wrote the manuscript. D.L. performed cryo-EM analysis. D.L. and T.S. analysed the data and co-wrote the manuscript. P.Y. conceived and supervised the study and wrote the paper. All authors reviewed, edited and approved the manuscript.

Competing interests

A patent based on this work[51] was issued to J.S., W.S. and P.Y.

Additional information

Extended data is available for this paper at https://doi.org/10.1038/s41563-021-00930-7.

Supplementary information The online version contains supplementary material available at https://doi.org/10.1038/s41563-021-00930-7.

Correspondence and requests for materials should be addressed to P.Y.

Reprints and permissions information is available at www.nature.com/reprints.

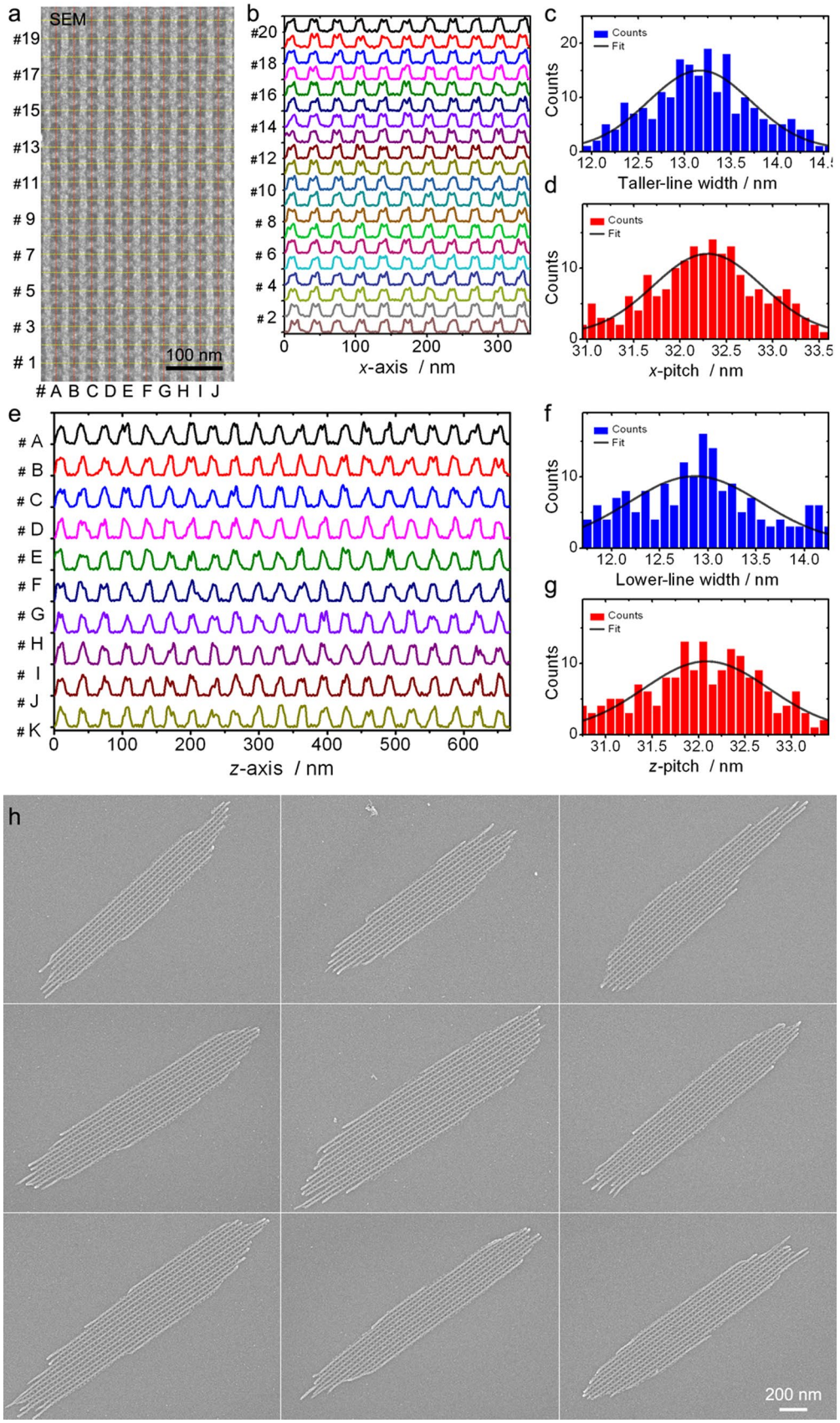

Extended Data Fig. 1 | Characterization of DNA mask 12H-grid. a, SEM image section of DNA mask 12H-grid. **b**, The corresponding SEM line-scan profiles along the *x* axis. **c**, The histogram of mask taller-line width. **d**, The histogram of taller-line pitch. **e**, The corresponding SEM line-scan profiles along the *z* axis. **f**, The histogram of mask lower-line width. **g**, The histogram of lower-line pitch. **h**, SEM images of randomly selected DNA mask 12H-grid.

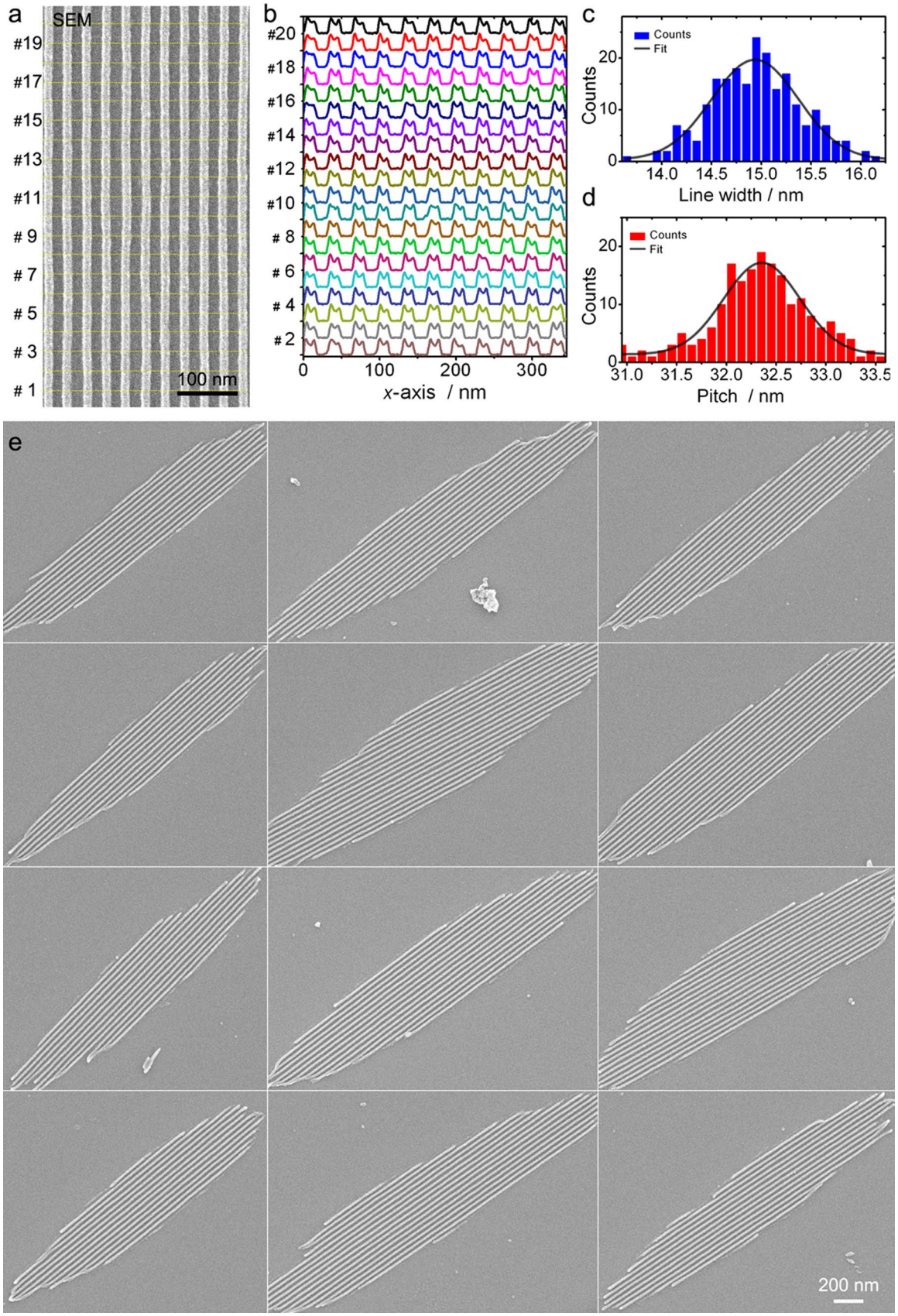

Extended Data Fig. 2 | Characterization of DNA mask 12H-b. a, SEM image section of DNA mask 12H-b with labeled scan-lines. **b**, The corresponding SEM line-scan profiles along the *x* axis. **c**, The histogram of DNA line width. **d**, The histogram of DNA line pitch. **e**, SEM images of randomly selected DNA mask 12H-b.

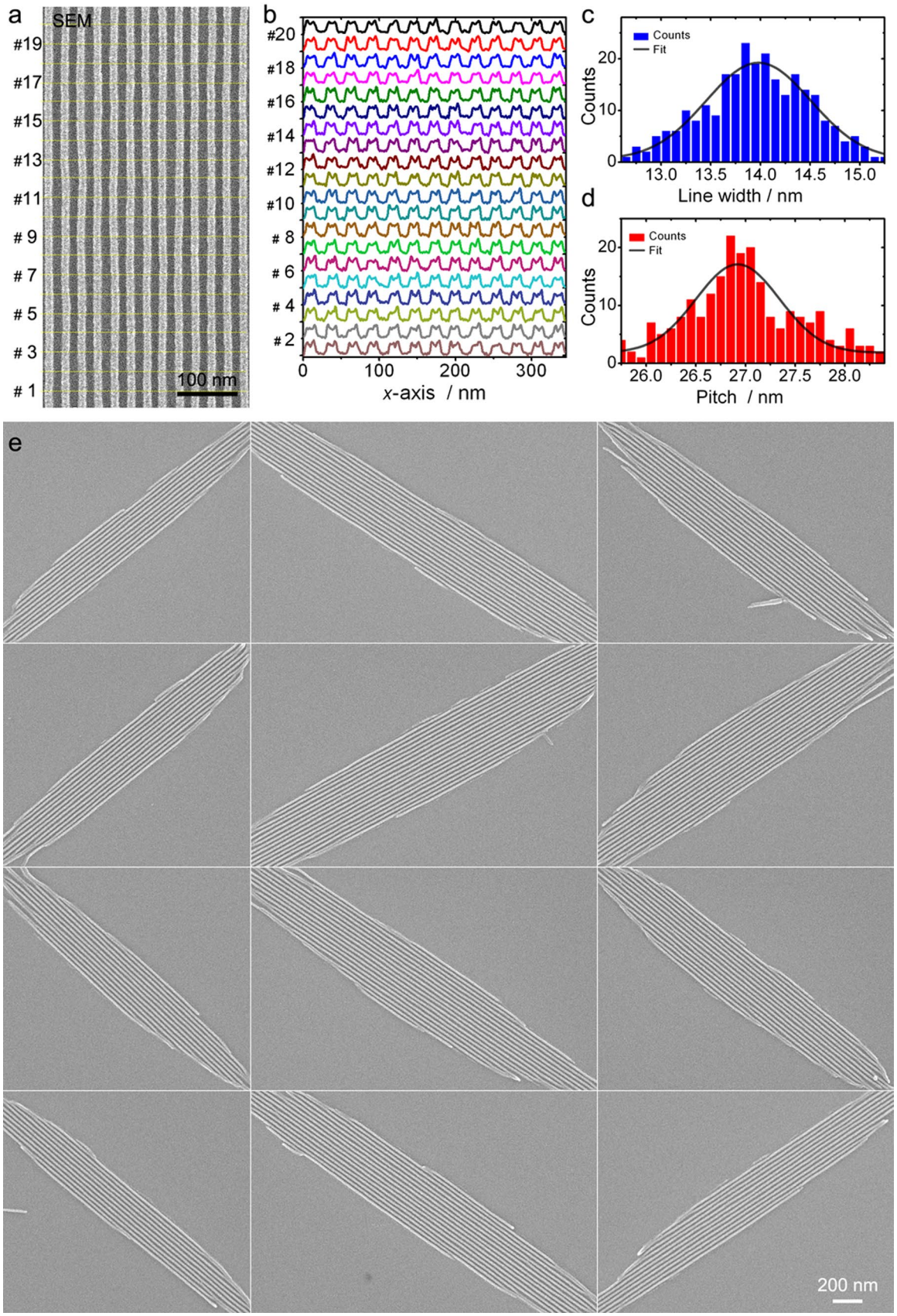

Extended Data Fig. 3 | Characterization of DNA mask 10H-b. a, SEM image section of DNA mask 10H-b with labeled scan-lines. **b**, The corresponding SEM line-scan profiles along the *x* axis. **c**, The histogram of DNA line width. **d**, The histogram of DNA line pitch. **e**, SEM images of randomly selected DNA mask 10H-b.

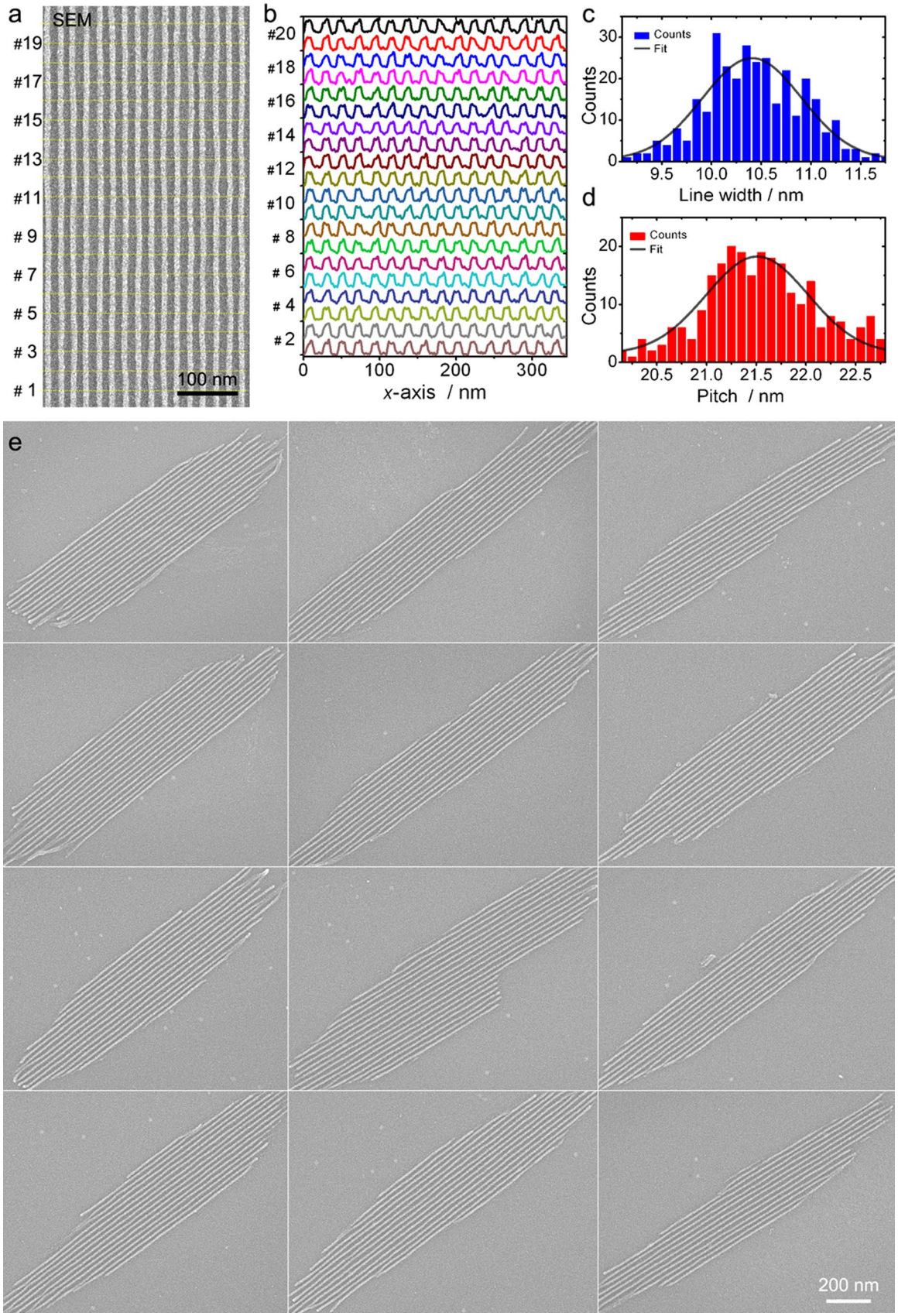

Extended Data Fig. 4 | Characterization of DNA mask 8H-b. a, SEM image section of DNA mask 8H-b-0.5H_2 with labeled scan-lines. **b**, The corresponding SEM line-scan profiles along the *x* axis. **c**, The histogram of DNA line width. **d**, The histogram of DNA line pitch. **e**, SEM images of randomly selected DNA mask 8H-b-0.5H_2.

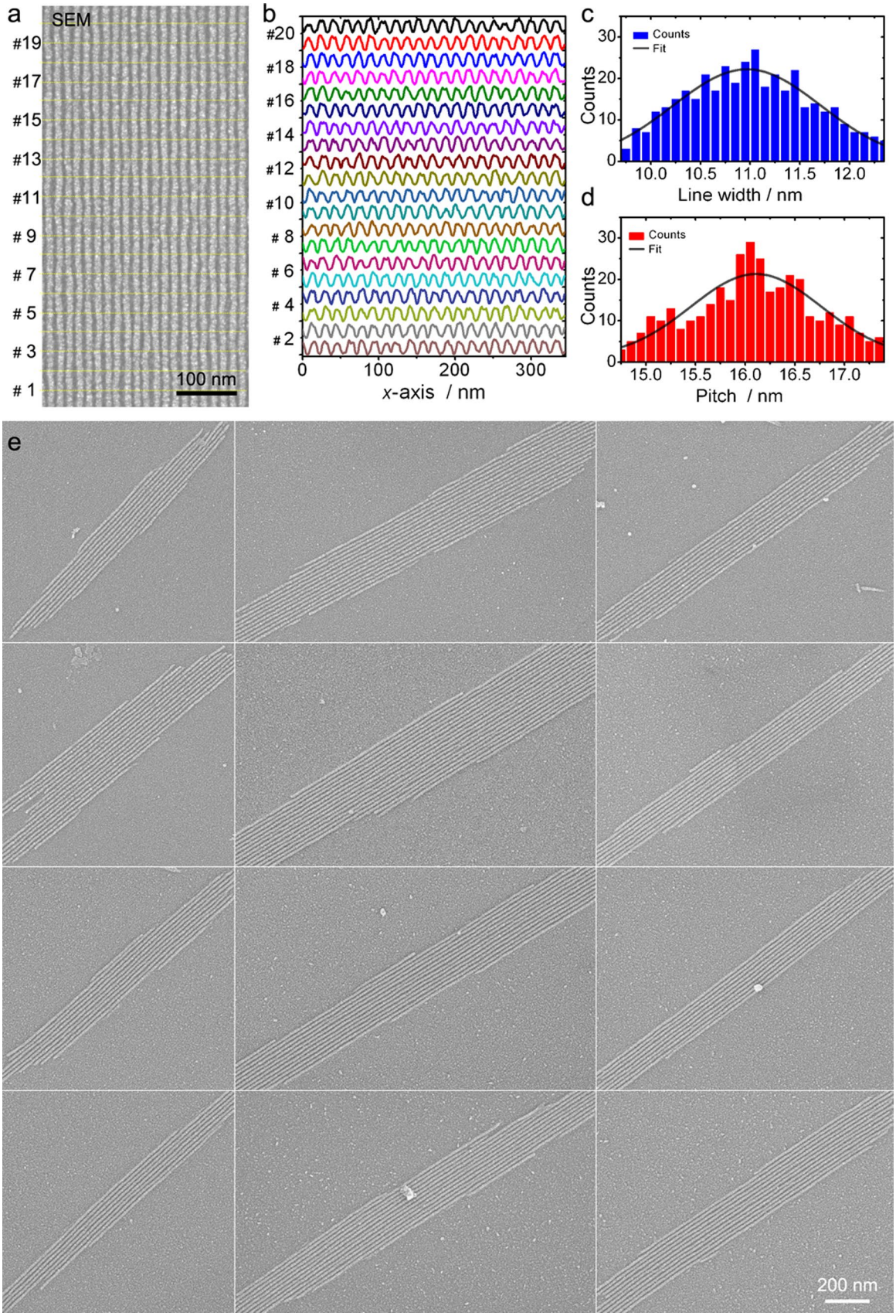

Extended Data Fig. 5 | Characterization of DNA mask 6H-b. a, SEM image section of DNA mask 6H-b with labeled scan-lines. **b**, The corresponding SEM line-scan profiles along the *x* axis. **c**, The histogram of DNA line width. **d**, The histogram of DNA line pitch. **e**, SEM images of randomly selected DNA mask 6H-b.

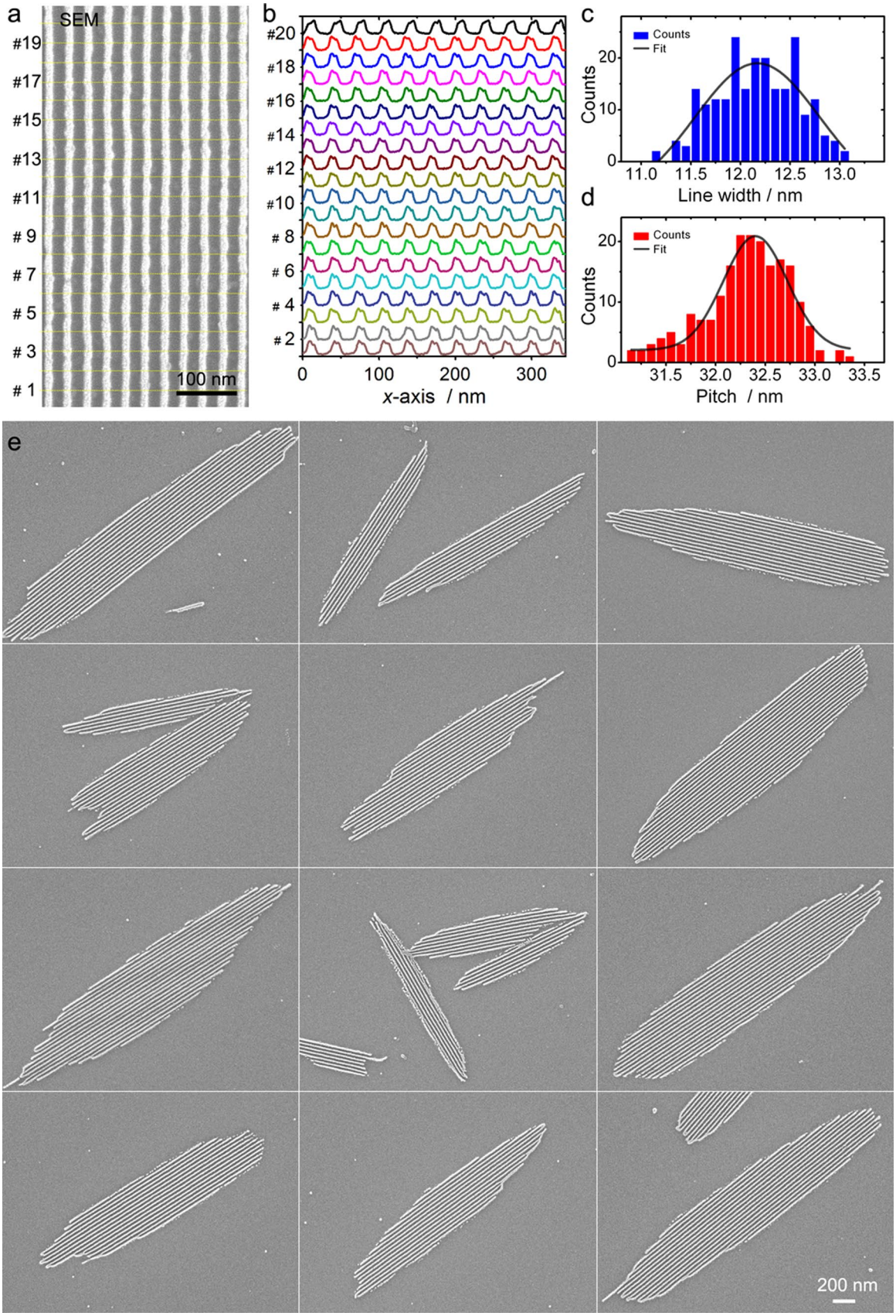

Extended Data Fig. 6 | Characterization of silicon pattern Si-12H-b. a, SEM image section of silicon pattern Si-12H-b with labeled scan-line profiles. **b**, The corresponding SEM line-scan profiles along the *x* axis. **c**, The histogram of silicon line width. **d**, The histogram of silicon line pitch. **e**, SEM images of randomly selected silicon pattern Si-12H-b.

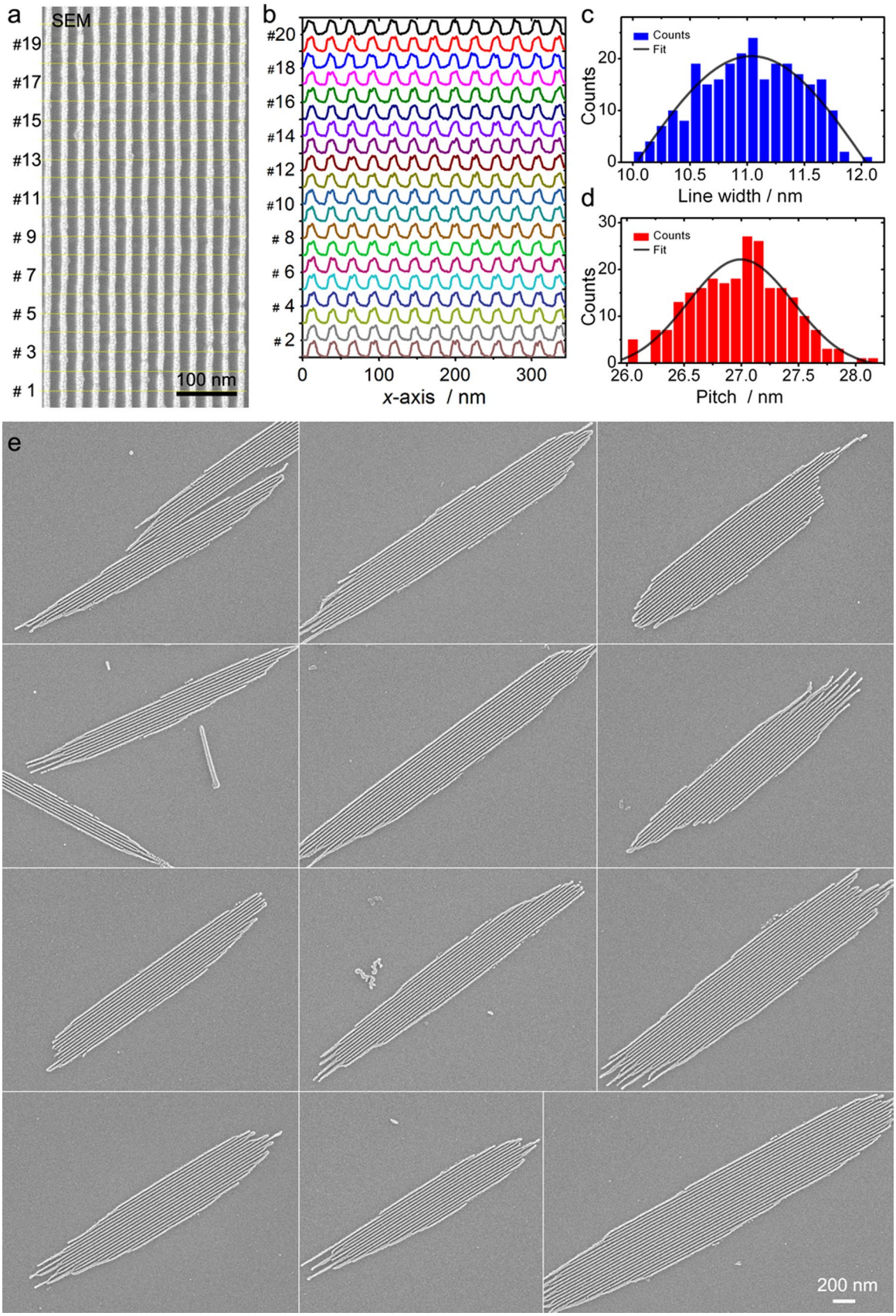

Extended Data Fig. 7 | Characterization of silicon pattern Si-10H-b. a, SEM image section of silicon pattern Si-10H-b with labeled scan-line profiles. **b**, The corresponding SEM line-scan profiles along the *x* axis. **c**, The histogram of silicon line width. **d**, The histogram of silicon line pitch. **e**, SEM images of randomly selected silicon pattern Si-10H-b.

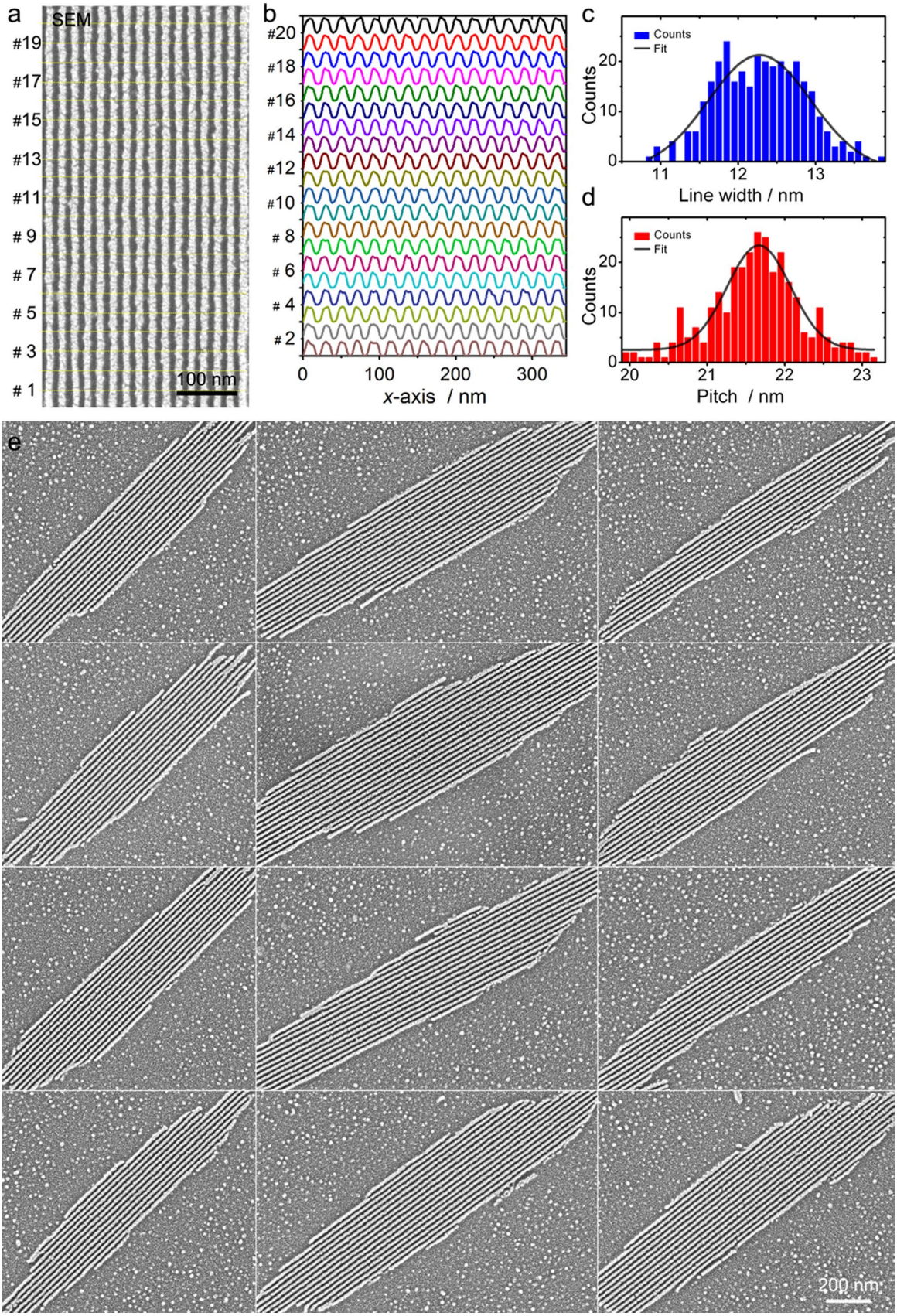

Extended Data Fig. 8 | Characterization of silicon pattern Si-8H-b-0.5H2. a, SEM image section of silicon pattern Si-8H-b-0.5H_2 with labeled scan-line profiles. **b**, The corresponding SEM line-scan profiles along the *x* axis. **c**, The histogram of silicon line width. **d**, The histogram of silicon line pitch. **e**, SEM images of randomly selected silicon pattern Si-8H-b-0.5H_2.

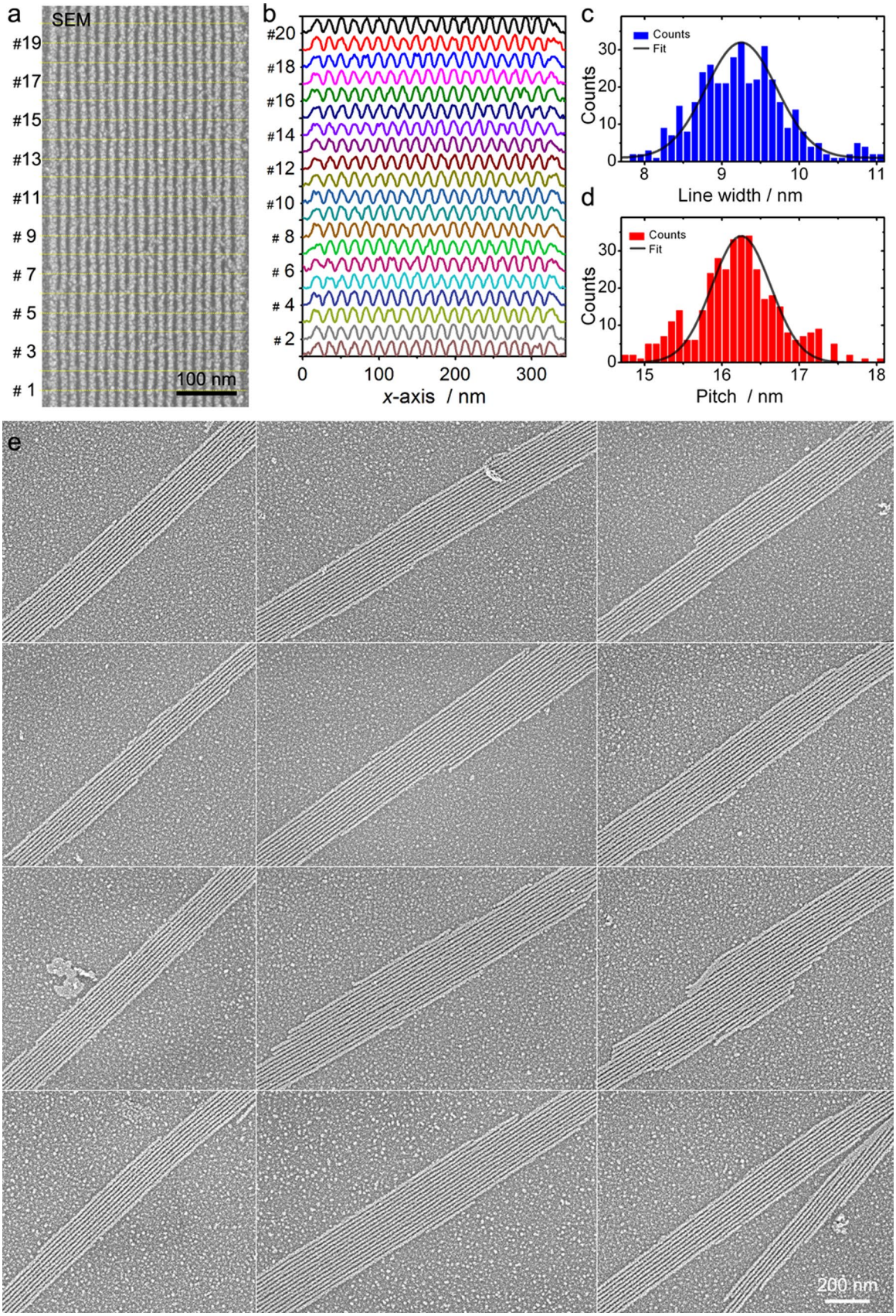

Extended Data Fig. 9 | Characterization of silicon pattern Si-6H-b. a, SEM image section of silicon pattern Si-6H-b with labeled scan-lines. **b**, The corresponding SEM line-scan profiles along the *x* axis. **c**, The histogram of silicon line width. **d**, The histogram of silicon line pitch. **e**, SEM images of randomly selected silicon pattern Si-6H-b.

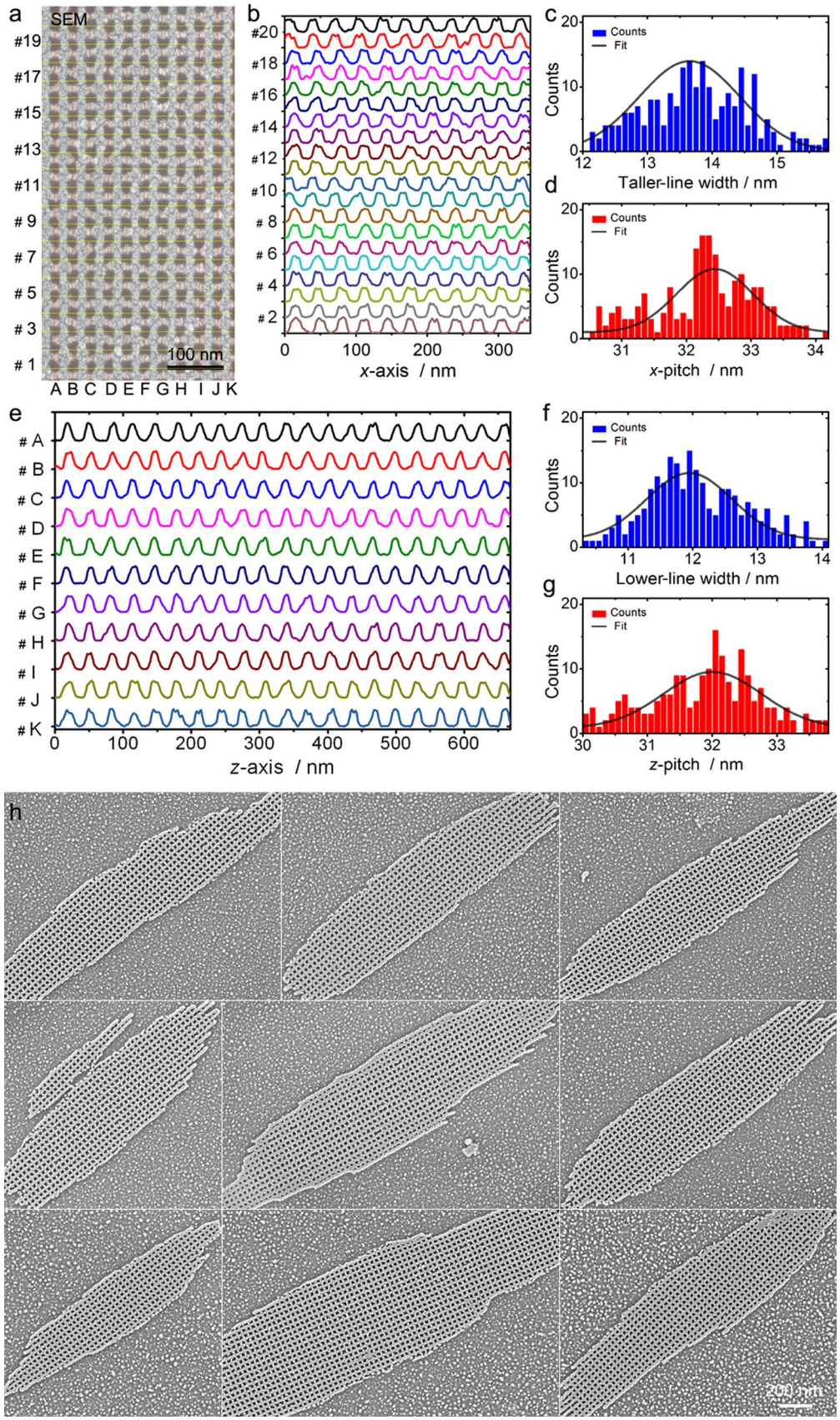

Extended Data Fig. 10 | Characterization of silicon pattern Si-12H-grid. a, SEM image section of silicon pattern Si-12H-grid. **b**, The corresponding SEM line-scan profiles along the *x* axis. **c**, The histogram of taller-Si-line width. **d**, The histogram of taller-Si-line pitch. **e**, The corresponding SEM line-scan profiles along the *z* axis. **f**, The histogram of lower-Si-line width. **g**, The histogram of lower-Si-line pitch. **h**, SEM images of randomly selected silicon pattern Si-12H-grid.